atmosphere

MDPI

Article

Improved Surface Soil Moisture Estimation Model in Semi-Arid Regions Using the Vegetation Red-Edge Band Sensitive to Plant Growth

Rencai Lin [1], He Chen [1], Zheng Wei [1,*], Yinong Li [1], Baozhong Zhang [1], Haoran Sun [2] and Minghan Cheng [3]

[1] State Key Laboratory of Watershed Water Cycle Simulation and Regulation, China Institute of Water Resources and Hydropower Research, Beijing 100048, China; rencaihrs@iwhr.com (R.L.); chenhe@iwhr.com (H.C.); liyinong@iwhr.com (Y.L.); zhangbz@iwhr.com (B.Z.)
[2] School of Spatial Information and Geomatics Engineering, Anhui University of Science and Technology, Huainan 232001, China; 2018200912@aust.edu.cn
[3] College of Agriculture Science and Engineering, Hohai University, Nanjing 210048, China; chengmh@hhu.edu.cn
* Correspondence: weizheng@iwhr.com; Tel.: +86-187-1004-7605

Abstract: Accurate description of surface soil moisture (SSM) in vegetation-covered areas is of great significance to water resource management and drought monitoring. To remove the effect of vegetation on SSM estimation, the vegetation index obtained from Sentinel-2 (S2) was applied for vegetation water content (VWC) estimation. The VWC model was substituted into the water cloud model (WCM), and thus, the SSM estimation model was developed based on the WCM. The methodology was tested at Daxing, Beijing, and Gu'an, Hebei, in which training and validation data of SSM were acquired by in situ measurements. The results can be described as follows: (1) For the vegetation-covered areas, the Modified Chlorophyll Absorption Ratio Index (MCARI) obtained from the B3, B4, and B5 bands of S2 was the most suitable for removing the influence of vegetation on SSM estimation; (2) Compared to Sentinel-1 (S1) vertical–horizontal (VH) polarization, vertical–vertical (VV) polarization was more suitable for SSM estimation and achieved higher accuracy; (3) The developed model could be used to estimate SSM under crop cover with high accuracy, which indicated the correlation coefficients (R^2) between in situ measured and estimated SSM were 0.867, the root mean square error (RMSE) was 0.028 cm^3/cm^3, and the MAE was 0.023 cm^3/cm^3. Thus, this methodology has the potential for SSM estimation in vegetated areas.

Keywords: Sentinel-1; Sentinel-2; surface soil moisture; water cloud model; red-edge band; vegetation water content

check for updates

Citation: Lin, R.; Chen, H.; Wei, Z.; Li, Y.; Zhang, B.; Sun, H.; Cheng, M. Improved Surface Soil Moisture Estimation Model in Semi-Arid Regions Using the Vegetation Red-Edge Band Sensitive to Plant Growth. *Atmosphere* **2022**, *13*, 930. https://doi.org/10.3390/atmos13060930

Academic Editor: Alexey V. Eliseev

Received: 6 May 2022
Accepted: 2 June 2022
Published: 7 June 2022

Publisher's Note: MDPI stays neutral with regard to jurisdictional claims in published maps and institutional affiliations.

Copyright: © 2022 by the authors. Licensee MDPI, Basel, Switzerland. This article is an open access article distributed under the terms and conditions of the Creative Commons Attribution (CC BY) license (https://creativecommons.org/licenses/by/4.0/).

1. Introduction

Surface soil moisture (SSM) is a vital parameter in many fields such as agriculture [1], meteorology [2], and hydrology [3]. It is widely used in drought monitoring, weather forecasting, and hydrology forecasting [4–6]. SSM, which is the content of water contained in 0–5 cm of the soil layer [7], is a vital index for crop yield estimation, pest and disease control, irrigation management, and land improvement in agricultural planting areas [8]. It is of great significance to obtain this parameter accurately for sustainable agricultural development [9]. SSM is also an important part of soil water content, which is the initial condition for the transportation of soil moisture and heat, leading to a great effect on the accuracy of soil moisture content simulation in the root zone. Traditional SSM monitoring methods, such as the weighing method and the time-domain reflectometry (TDR) method [10,11], have accurate monitoring data, but they consume a lot of human capital, material resources, and financial resources. A more serious problem is its inability to meet regional monitoring objectives [12]. With the progress of remote sensing science and technology, regional SSM monitoring has become possible, and the accuracy of estimation

is constantly being improved. It has become one of the indispensable means of regional soil moisture monitoring [13–17]. Remote sensing methods include two categories, namely optical and microwave remote sensing. Optical remote sensing is susceptible to cloud, fog, rain, and ground vegetation, which often leads to poor data quality and low availability, especially in southern China. Thus, optical remote sensing methods are generally applicable only for SSM estimation in bare or free vegetation-covered areas and under good weather conditions. In contrast, microwave remote sensing at longer wavelengths has a stronger penetrating ability that is not affected by meteorological conditions. It can be used to monitor various surface parameters, including SSM, over vegetated areas [18] and has certain advantages in SSM estimation [19].

Sentinel-1 (S1), which can provide near-real-time synthetic aperture radar (SAR) images, is widely used in agricultural monitoring. Based on S1 SAR images, Paloscia et al. [20] developed an SSM mapping algorithm based on the artificial neural network (ANN) method. The results showed that the validation results were very much in line with the Global Monitoring for Environment and Security (GMES) requirements, which indicated a good correlation between estimated and in situ measured SSM values. Li et al. [21] presented an improved convolutional neural network (ICNN) method through combined multipolarized SAR and original multispectral images, which achieved regional SSM information with an average root mean square error (RMSE) of 0.0145 cm^3/cm^3. Most of the developed methods can achieve desirable results in bare or sparse vegetation-covered areas, but the precision is not ideal for SSM estimation in vegetated areas. The water cloud model (WCM) is a commonly used semi-empirical model for SSM retrieval in vegetated areas [22]. Based on the WCM, previous studies [23,24] estimated SSM from C- and X-band SAR with an accuracy better than 8 vol%. Rawat et al. [25] used S1 and Landsat-8 images to retrieve SSM over vegetated areas based on the modified water cloud model (MWCM). The results showed a good correlation between estimated and in situ measured SSM.

In the WCM, the backscattering coefficient includes soil contribution and direct vegetation contribution. The vegetation backscattering coefficient is calculated by one or more vegetation descriptors. The vegetation water content (VWC) is one of the most vital parameters in the WCM. To remove the effect of vegetation on SSM estimation, it is necessary to obtain the VWC. Numerous studies [26–28] have indicated the application of the Normalized Difference Vegetation Index (NDVI), as the vegetation descriptor allows for the calculation of the vegetation backscattering coefficient on the total backscattering coefficient with good accuracy. In addition, some studies [29–31] have demonstrated that the Normalized Difference Water Index (NDWI) can be used for VWC estimation instead of measuring by manual work. However, the NDVI is limited to a certain range of vegetation coverage, and the NDWI has a poor ability to remove the effect of background soil reflectance, although the NDVI and NDWI can reduce the effect of vegetation coverage. The Chlorophyll Absorption Ratio Index (CARI) measures the depth of chlorophyll absorption at 670 nm relative to the green reflectance peak at 550 nm and the reflectance at 700 nm to describe the chlorophyll content of vegetation. Daughtry et al. [32] developed the Modified Chlorophyll Absorption Ratio Index (MCARI) based on the CARI, mainly by increasing the R_{700}/R_{670} ratio, in an attempt to minimize the influence of soil reflectance and canopy nonphotosynthetic substances. Chlorophyll is a plant biochemical parameter that is closely related to nitrogen, cellulose, water, and other vegetation biochemical parameters [33]. At present, there are few reports on VWC estimation using this index, and its potential for soil moisture estimation needs to be further explored. Therefore, we attempted to use the MCARI to describe the VWC and remove the effect of vegetation on SSM estimation in order to make positive contributions to agricultural water resource management and drought monitoring.

Based on S1 SAR and S2 MSI data, this study took farmland in Daxing, Beijing, and Gu'an, Hebei, China, as the study area. Aiming at the problem that the sensitivity of radar signals in farmland vegetation coverage decreases in SSM estimation, a planting cover index was introduced, namely the MCARI. In this paper, a semi-empirical model of

SSM estimation in a vegetation-covered area based on microwave and optical RS data was developed, and soil moisture inversion experiments under six inversion modes formed by the combination of the vegetation indices (NDVI, NDWI, and MCARI) and the polarization modes (VV and VH) were carried out to analyze the robustness of the proposed model, which provides a research idea for the cooperative inversion of SSM in vegetation-covered areas. The method was tested in semi-arid farmland crop cover areas in Daxing, Beijing, and Gu'an, Hebei, China.

2. Data and Methodology

2.1. Study Area

The Haihe basin is located in North China (35° N–3° N, 112° E–120° E), with an area of 318,000 km^2 [34]. It meets the needs of around 10% of China's population and contributes about 8% of cultivated land in China. Corn and wheat are widely cultivated in the basin. The agricultural production of corn and wheat accounts for 36% and 27% of the total panting area [35], respectively. The study area is located in the middle of the Haihe basin and covers an area of 1728 km^2 (Figure 1). It has a sub-humid monsoon climate with an elevation of 14–52 m. The annual average temperature is 11.6 °C, and the annual average precipitation is 556 mm. The rainfall in July, August, and September accounts for 60–70% of the annual total precipitation. The soil types in the study area are mostly loam and sandy loam, and the main crops are winter wheat and summer corn. The growth period of winter wheat is from March to May, and summer corn is grown from July to September.

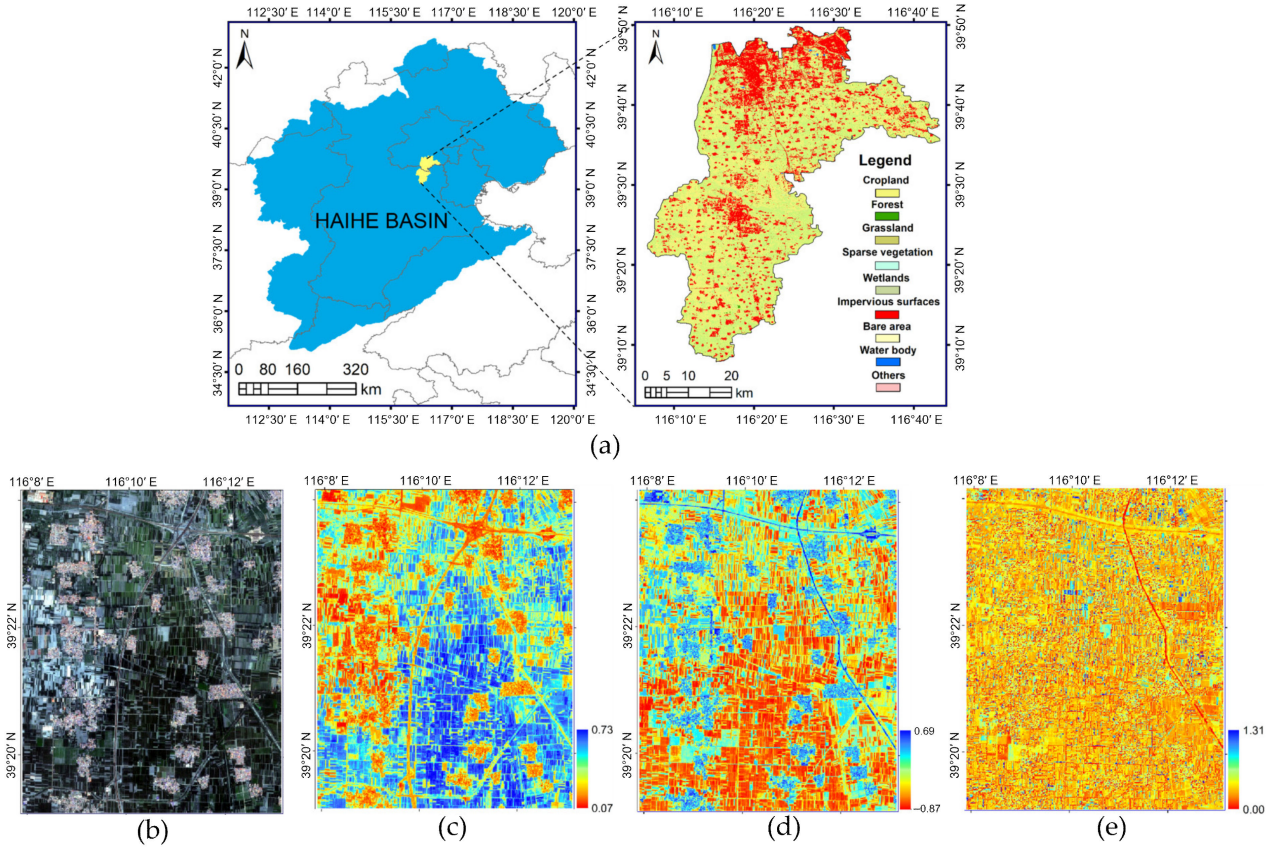

Figure 1. Satellite data of the study area: (**a**) relative location of the study area; (**b**) S2 image (in false-color composite: R = NIR, G = red, B = green), sample area from the study area; (**c**) NDVI calculated from an S2 image, sample area from the study area; (**d**) NDWI calculated from an S2 image, sample area from the study area; (**e**) MCARI calculated from an S2 image, sample area from the study area.

2.2. Data Sets

2.2.1. Sentinel-1

Sentinel-1 (S1) is a vital component of the Global Monitoring for Environment and Security (GMES) proposed by the European Space Agency (ESA). It includes two satellites, namely Sentinel-1A and Sentinel-1B, which were successfully launched on 3 April, 2014, and 25 April, 2016, respectively. The time resolution of a single satellite is 12 days, which decreases to 6 days after two satellites are networked. S1 is equipped with a C-band SAR sensor and has two kinds of VV and VH polarization, with a working frequency of 5.4 GHz. There are four data acquisition modes (Table 1). The S1 images used in our research are Level 1 products with a single-look complex (SLC) format from an IW mode. Two S1 images were obtained on 28 April 2019 and 29 April 2021 from the ESA (https://scihub.copernicus.eu/) to test the developed SSM estimation method (Table 2). The obtained S1 SAR images needed to be preprocessed before being analyzed. The SARscape 5.2.3 software was applied to conduct the radiometric calibration and geocoding to obtain the backscattering coefficient. The backscatter radiation was calculated from previously calibrated S1 images and converted to decibels (dB) by the transformation relation [13]:

$$\sigma^0(dB) = 10\log_{10}\left(\sigma^0\right) \quad (1)$$

Table 1. Characteristics of the various imaging modes of S1 image.

Mode	Incident Angle (°)	Spatial Resolution	Width (km)
MW	22–38	5 m × 5 m	20 × 20
EW	19–47	20 m × 40 m	400
IW	29–45	5 m × 20 m	250
SM	20–45	5 m × 5 m	80

Table 2. S1 images used in this research.

ID	Data of Acquisition (D/M/Y)	Mean Incidence Angle (°C)	Imaging Model	Polarization
D1	28 April 2019	38.85	IW	VV/VH
D2	29 April 2021	38.85	IW	VV/VH

2.2.2. Sentinel-2

Sentinel-2 (S2) contains two satellites (Sentinel-2A and Sentinel-2B), both carrying a multispectral imager (MSI) with a bandwidth of 290 km. The S-2A satellite carries an innovative wide-swath high-resolution multispectral imager with 13 spectral bands. These working bands have three different geometric resolutions ranging from 10 to 60 m, specifically, high-resolution visible images (red, green, blue, and near-infrared bands), with a 10 m ground sample distance (GSD), and red-edge, narrow near-infrared, and shortwave infrared bands with a 20 m GSD. With the launch of Satellite S-2B, the two sensors in orbit have significantly shortened the revisit time, resulting in a 5-day interval for S2 images. Its superiority in spatiotemporal resolution provides adequate and high-quality data in areas, facilitating the broad application of satellite images. S2 images are provided freely for users through the United States Geological Survey (USGS) (https://glovis.usgs.gov/). Optical RS images of the study site were obtained from Sentinel-2A on dates 25 April 2019 and 27 April 2021, which are close to those of the S1 images acquired (28 April 2019 and 29 April 2021). In theory, it is possible to obtain one S1 image and one S2 image with a difference in time of less than one week because, in agricultural areas, the vegetation does not change much within one week [36]. The obtained S2 images need to be processed before being analyzed. S2 Level 1C images (S2 L1C) were selected, to which geometric correction and radiometric correction were made. The Sentinel Application Platform (SNAP) was used to

treat it as an L2A product. Based on the S2 images, image registration was performed on S1 and S2 data after pretreatment.

2.2.3. In Situ Measurements

In this research, in situ experiments were designed on 28 April 2019 and 29 April 2021. The soil volumetric moisture at a 0–5 cm depth was obtained by handheld TDR. A total of 172 experimental points (91 points were used for model building, and 81 points were used for validation) were set up on both dates, with a reasonable spatial distribution. A detailed distribution of the experimental points is displayed in Figure 2a. The soil volumetric moisture content on every experimental point was obtained from the average of three measuring points, which were arranged within a radius of 3 m from the experimental point. A portable global positioning system (GPS) receiver was used for positioning measurement. Figure 3 shows the statistics of the 172 in situ measured SSM values. As shown in Figure 3a, the in situ measured SSM values range between 0.05 and 0.32 cm^3/cm^3. The mean, maximum, and minimum values of the in situ measured SSM were 0.169, 0.32, and 0.05 cm^3/cm^3, respectively. The measurements collected for wheat, corn, vegetables, soybean, and sweet potato were 82, 50, 24, 10, and 6, respectively.

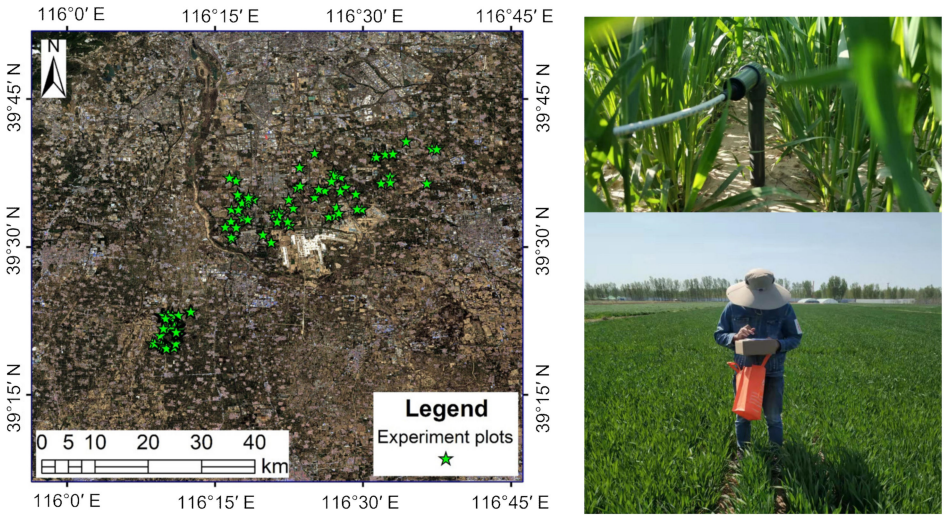

Figure 2. Basic information of in situ measurements: (**a**) distribution of experimental plots in the study area; (**b**) photograph of the scene.

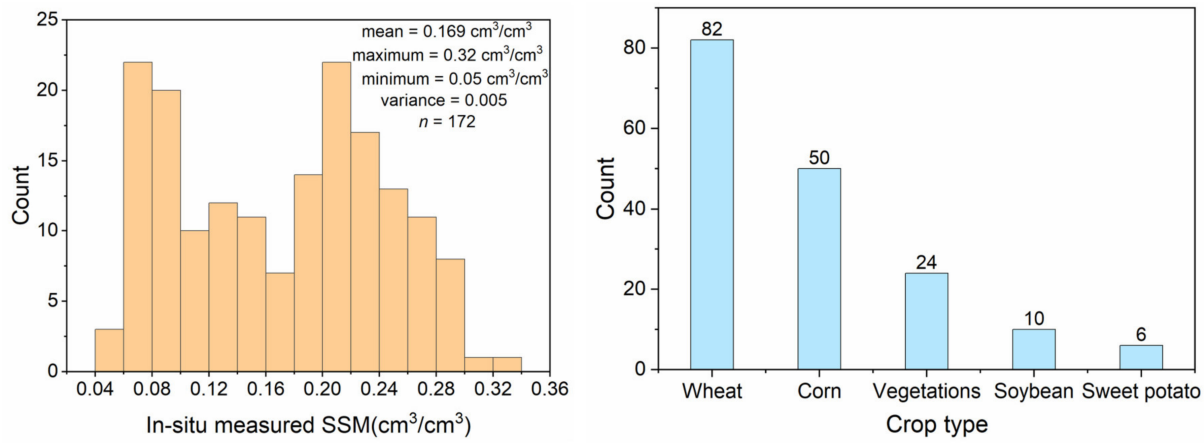

Figure 3. Statistics of in situ measured SSM: (**a**) distribution of in situ measured SSM; (**b**) in situ measurements for different crop types.

2.3. Methodology

The workflow of our research is illustrated in Figure 4. First, the downloaded S1 images were preprocessed, and the backscattering coefficient images in the study area were obtained. Second, the backscattering coefficients of each sample were extracted according to the latitude and longitude. Third, the downloaded S2 images were preprocessed, and the spectral index images covering the study areas were obtained. Moreover, the vegetation indices of each sample were extracted according to the latitude and longitude coordinates. In order to eliminate the influence of vegetation on SSM inversion, the VWC estimation model was established by using the S2 spectral index. This model was substituted into the original WCM, and an improved WCM with the spectral index was established. Finally, the SSM estimation model was developed based on the improved WCM.

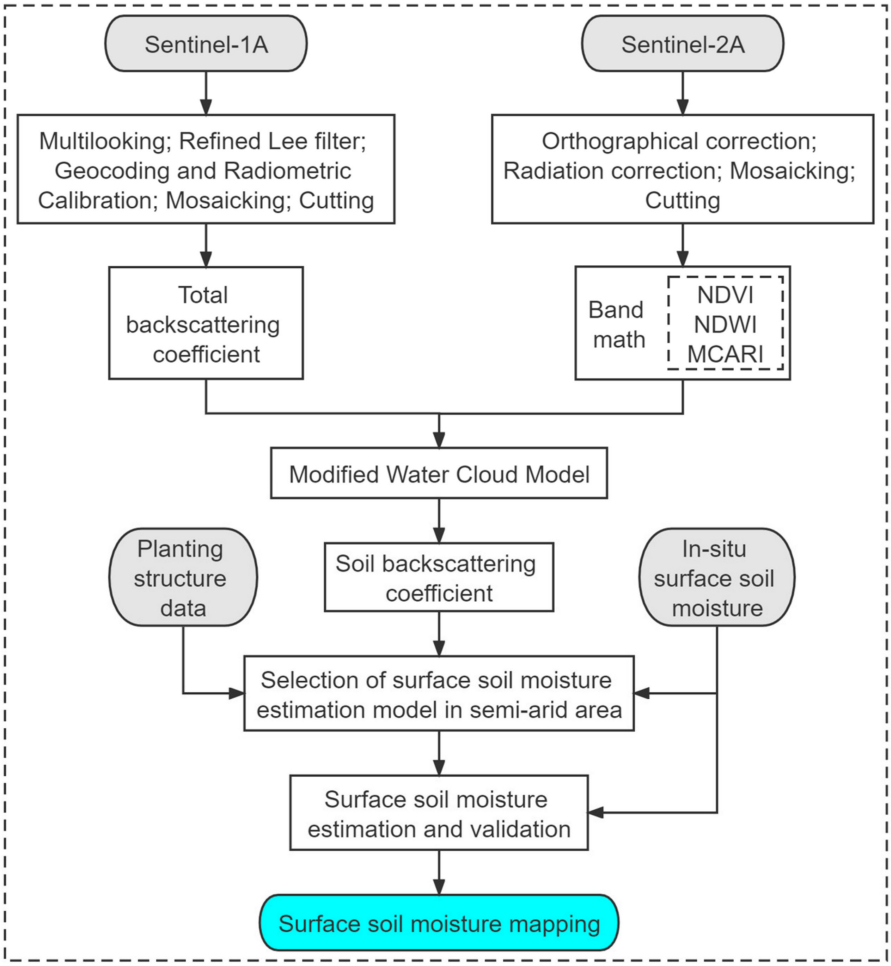

Figure 4. Workflow of this research.

2.3.1. Water Cloud Model

To distinguish the backscattering of soil and vegetation in the vegetated areas, the WCM developed by Attema and Ulaby [22] was adopted in our research. The WCM is based on the radiative transfer model, assuming that the vegetation canopy is a uniform horizontal cloud layer, ignoring multiple scattering between the vegetation and the surface. In the WCM, the scattering of the vegetated areas can be divided into two parts: one is the backscattering reflected directly by the vegetation, and the other is the scattering from the soil [17]. The model is simple and practical in describing radar scattering mechanisms in

vegetated areas. Thus, this model has often been used for relevant information estimation in vegetated areas. The WCM is expressed as:

$$\sigma^0 = \sigma^0_{veg} + T^2\sigma^0_{soil} \tag{2}$$

$$\sigma^0_{veg} = AM_v\cos(\theta)\left(1 - T^2\right) \tag{3}$$

$$T^2 = \exp(-2BM_v\sec(\theta)) \tag{4}$$

In addition, the term $\exp(-2BM_v\sec(\theta))$ was described with the Taylor formula:

$$\exp(-2BM_v\sec(\theta)) = 1 - 2BM_v\sec(\theta) + 2B^2{M_v}^2\sec^2(\theta) + \cdots \tag{5}$$

where σ^0 is the total backscattering coefficient, dB; σ^0_{veg} is the vegetation backscattering coefficient, dB; σ^0_{soil} is the soil backscattering coefficient, dB; M_v is the VWC, kg/m^2; T^2 is the double attenuation factor; θ is the incident angle, °; A is the vegetation reflectance; and B is the attenuation factor.

2.3.2. Vegetation Water Content Estimation

The VWC is the most vital parameter in the WCM. To remove the effect of vegetation on SSM estimation, the VWC needs to be calculated. Published studies [26,36,37] have indicated the spectral indices calculated from remote sensing images can be used for VWC estimation. The spectral indices commonly include NDVI, NDWI, and MCARI. The calculation formulas are as follows:

$$\text{NDVI} = \frac{R_{nir} - R_{red}}{R_{nir} + R_{red}} = \frac{R_{b8} - R_{b4}}{R_{b8} + R_{b4}} \tag{6}$$

$$\text{NDWI} = \frac{R_{nir} - R_{swir}}{R_{nir} + R_{swir}} = \frac{R_{b8} - R_{b11}}{R_{b8} + R_{b11}} \tag{7}$$

$$\text{MCARI} = \left[\left(R_{veg-red} - R_{red}\right) - 0.2\left(R_{veg-red} - R_{green}\right)\right] \times \frac{R_{veg-red}}{R_{red}} = \left[(R_{b5} - R_{b4}) - 0.2(R_{b5} - R_{b3})\right] \times \frac{R_{b5}}{R_{b4}} \tag{8}$$

where R_{nir} is the reflectance of the near-infrared band, R_{red} is the reflectance of the red band, R_{blue} is the reflectance of the blue band, R_{swir} is the reflectance of the shortwave infrared band, and R_{bx} is the reflectance of the x-band of the S2 satellite.

It was demonstrated that the relationship between the VWC and vegetation indices is linear, one-variable quadratic, or exponential [38,39]. Considering that the study area is flat and the influence of soil roughness is not taken into account, the land cover is mainly farmland, which is similar to the research conditions carried out by Bao et al. [40] in Spain and the UK. Therefore, the VWC can be expressed as follows:

$$M_v = a \cdot \text{VI}^2 + b \cdot \text{VI} + c \tag{9}$$

2.3.3. Algorithm of SSM Estimation

The backscattering coefficient is sensitive to the surface dielectric constant and is closely related to SSM. A previous study [41] has shown there is a good linear correlation between the soil backscattering coefficient (σ^0_{soil}) and SSM. Thus, the σ^0_{soil} can be expressed as follows:

$$\sigma^0_{soil} = d \cdot \text{SSM} + e \tag{10}$$

where, d and e are the parameters of the soil. To build the SSM estimation model, Equations (9) and (10) were substituted into the WCM. Finally, the SSM estimation model was established:

$$\text{SSM} = l_1 + l_2\sigma^0 + l_3\text{VI} + l_4\text{VI}^2 + l_5\text{VI}^3 + l_6\text{VI}^4 + l_7\sigma^0\sec\theta + l_8\sigma^0\text{VI}\sec\theta + l_9\sigma^0\text{VI}^2\sec\theta \tag{11}$$

where SSM is the surface soil moisture, cm^3/cm^3; σ^0 is the VV or VH backscattering coefficients, dB; VI is the vegetation index calculated from S2 images; θ is the S1 incident angle (°); and l_1–l_9 could be obtained by the method of the best-fitting regression.

2.3.4. Statistical Metrics

To fully evaluate the performance of the estimated SSM, three metrics were used, including the determination coefficients (R^2), the mean absolute error (MAE), and the root mean square error (RMSE). The R^2 indicates the fit degree of the model, and the larger the R^2, the better the fitting effect, and the stronger the robustness of the model. The RMSE indicates the prediction accuracy of the model, and the smaller the RMSE, the higher the prediction accuracy of the model. The MAE is the average of the absolute value of the deviation between all individual measured values and estimated values. Compared with the mean error, the MAE will not be offset by positive and negative because the deviation is absolute. Therefore, the MAE can better reflect the actual situation of the predicted error, and the smaller the MAE, the better fitting effect of the model.

The statistical metrics are calculated as follows:

$$R^2 = \frac{\sum_{i=1}^{n} \left(S_i - \overline{S}\right)^2}{\sum_{i=1}^{n} \left(M_i - \overline{S}\right)^2} \tag{12}$$

$$MAE = \frac{1}{n}\sum_{i=1}^{n}|S_i - M_i| \tag{13}$$

$$RMSE = \sqrt{\frac{1}{n}\sum_{i=1}^{n}(S_i - M_i)^2} \tag{14}$$

where n is the number of validation values during the day, and M_i and S_i are the in situ measured and estimated SSM, respectively.

3. Results

3.1. SSM Estimation from Sentinel-1 Images

The established semi-empirical model was used to estimate the SSM values from the S1 SAR images combining the S2 vegetation indices. A simulated data set was established based on the WCM, and SSM was estimated by six modes of different polarization (VV and VH) and different vegetation indices (NDVI, NDWI, and MCARI). Figure 5 shows SSM mopping in a sample area. Nonagricultural land, such as buildings and roads, has a good removal effect (Figure 5). The variation trend of SSM obtained by the six modes was consistent in the same space. Figure 5d shows the highest SSM values, while Figure 5c shows the lowest. For the same vegetation index, the SSM values obtained by VH polarization were generally higher than those of VV polarization. Under the same polarization mode, the trend of SSM values obtained by the different vegetation indices is basically the same, which can be clearly seen in the circled part in Figure 5. Under VH polarization, the SSM values obtained by the different indices showed NDVI > NDWI > MCARI. However, under VV polarization, the SSM values obtained by the different indices showed little difference.

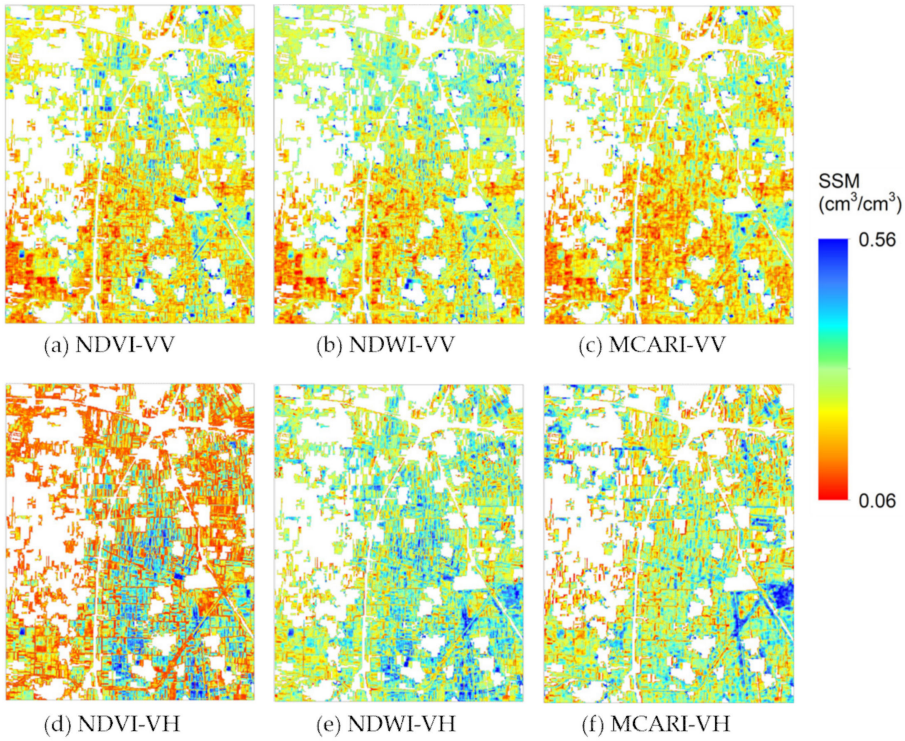

Figure 5. SSM mapping in a sample in Gu'an, Hebei.

Table 3 shows the estimation equation and accuracy of the model under the different polarization modes (VV and VH) and different indices (NDVI, NDWI, and MCARI). The number of training sets of the model is 91, and the fitting equations in the table are obtained by the least-squares method. As shown in Table 3, compared with the performances of S1 VV and VH polarization on SSM estimation, VV polarization obtained higher accuracy, and the accuracies obtained by NDVI, NDWI, and MCARI were 0.565, 0.576, and 0.588, respectively. Compared with S1 VV polarization, the accuracy of VH polarization was 0.2 lower. The accuracies of NDVI, NDWI, and MCARI were 0.336, 0.329, and 0.385, respectively. According to the fitting effect, it is preliminarily judged that the combination of the VV polarization mode and MCARI is most consistent with the real situation.

Table 3. Estimation equations and accuracy of SSM under different polarization and vegetation indices.

Polarization	Vegetation Index	N	Fitting Equation	R^2
VV	NDVI	91	$SSM = 0.399 - 0.367VI + 0.315VI^2 + 0.855VI^4 + 0.008\sigma^0 \sec\theta - 0.024\sigma^0 VI \sec\theta + 0.041\sigma^0 VI^2 \sec\theta$	0.565
	NDWI	91	$SSM = 0.208 - 1.159VI - 2.745VI^2 + 3.671VI^4 + 0.021\sigma^0 \sec\theta + 0.081\sigma^0 VI \sec\theta + 0.1\sigma^0 VI^2 \sec\theta$	0.576
	MCARI	91	$SSM = 0.313 + 2.506VI - 14.595VI^2 + 66.472VI^4 + 0.003\sigma^0 \sec\theta + 0.09\sigma^0 VI \sec\theta - 0.381\sigma^0 VI^2 \sec\theta$	0.588
VH	NDVI	91	$SSM = 0.939 - 3.45VI + 4.658VI^2 + 0.136VI^4 + 0.015\sigma^0 \sec\theta - 0.072\sigma^0 VI \sec\theta + 0.102\sigma^0 VI^2 \sec\theta$	0.336
	NDWI	91	$SSM = -0.232 - 2.727VI - 3.477VI^2 + 2.884VI^4 - 0.0000676\sigma^0 \sec\theta + 0.022\sigma^0 VI^2 \sec\theta$	0.329
	MCARI	91	$SSM = 0.427 + 4.289VI - 25.377VI^2 + 89.291VI^4 + 0.004\sigma^0 \sec\theta + 0.104\sigma^0 VI \sec\theta - 0.503\sigma^0 VI^2 \sec\theta$	0.385

3.2. Validation of SSM Estimation Model

To evaluate the robustness of the SSM estimation model, 81 in situ measurement points were selected to verify the model. The agreement between the estimated SSM values and

in situ measured SSM values was evaluated on the basis of statistical metrics, i.e., R^2, MAE, and RMSE. The estimated values of the six models were compared with in situ measured SSM, and the R^2, MAE, and RMSE were calculated (Figure 6). In VH polarization, the predicted SSM values were higher than the in situ measured results, and the scattered points were separated from the attachment of the 1:1 line. The predicted results of VV polarization were close to the in situ measured SSM values, and most of the scattered points were located near the 1:1 line.

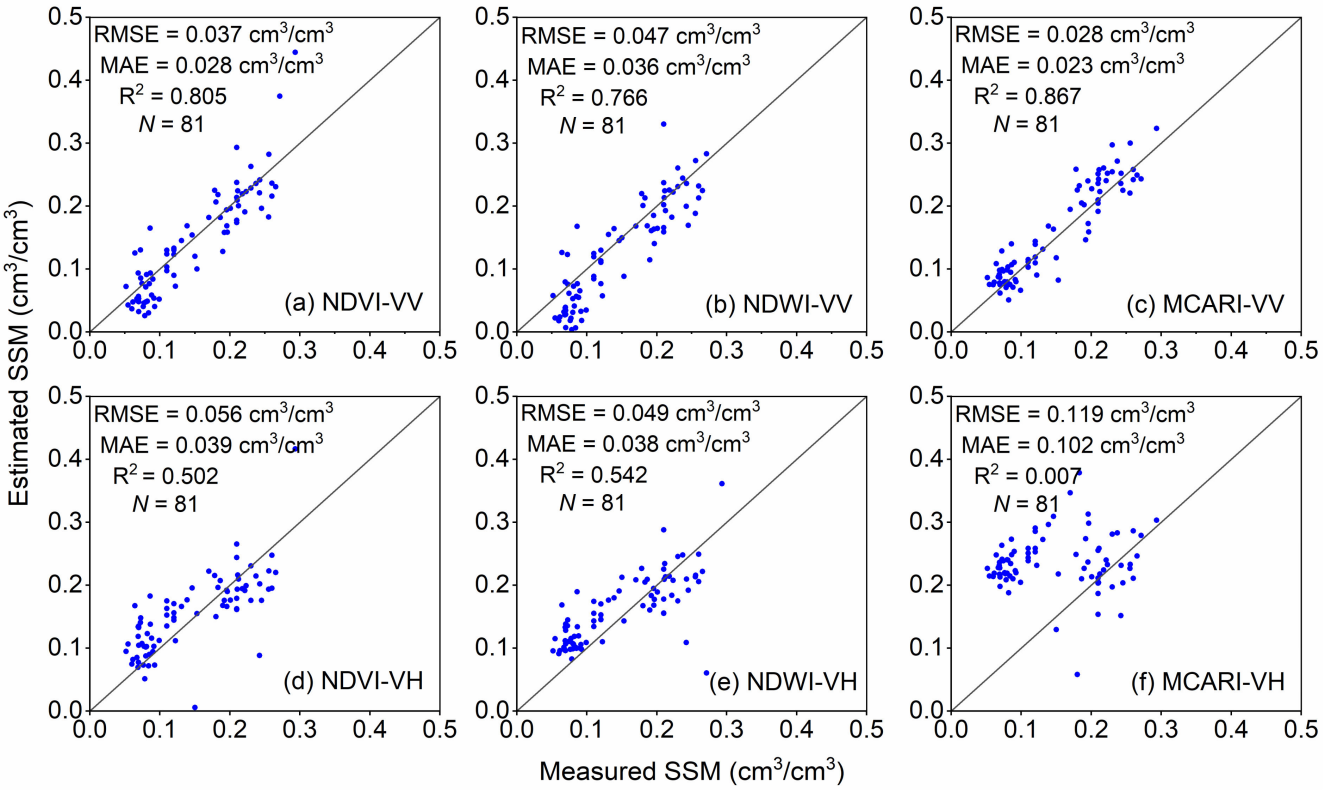

Figure 6. SSM validation under six models.

By comparing the R^2, MAE, and RMSE of the six SSM estimation models with the measured values, it can be seen that the combined effect of VV polarization and MCARI is the best. As seen in Figure 6c, the best performance is the combination of VV polarization and MCARI, with RMSE, MAE, and R^2 of 0.028 cm^3/cm^3, 0.023 cm^3/cm^3, and 0.867, respectively. Compared to the republished research [42] using single RS data, the method of combining the S1 and S2 images acquired higher accuracy. In summary, we chose MCARI and VV polarization to estimate SSM in our study.

3.3. Application of the SSM Estimation Model

The model was used to estimate regional SSM from the S1 SAR and S2 MSI images in the vegetation-covered area under clear-sky conditions. Figure 7a,b shows the SSM (20 m × 20 m) maps in Daxing on 28 April 2019 and 29 April 2021, respectively. The spatial distribution of the estimated SSM has large variability with a range of 0–0.49 cm^3/cm^3, mainly distributed between 0.12 and 0.28 cm^3/cm^3 (Figure 7a). There were no significant drought events or other extreme weather events. As seen in Figure 7b, the fields are slightly wetter than in Figure 7a. The estimated SSM is below 0.44 cm^3/cm^3, and the eastern part is wet. This can provide valuable reference information for various types of applications, especially for water resource management.

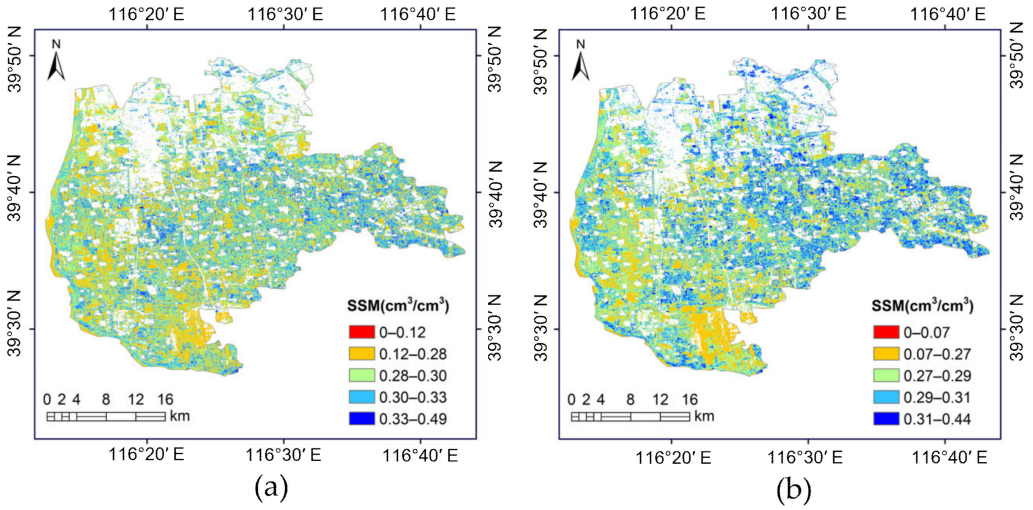

Figure 7. SSM mapping on two different dates: 28 April 2019 (**a**), and 29 April 2021 (**b**), in Daxing, Beijing, China.

Figure 8a,b shows the SSM maps in Gu'an on 28 April 2019 and 29 April 2021, respectively. As seen in Figure 8a, SSM is distributed from 0.09 to 0.46 cm^3/cm^3, the western part of Gu'an is relatively dry, while the southern part is relatively dry. As seen in Figure 8b, the fields are slightly droughter in most areas. SSM is below 0.40 cm^3/cm^3, but in most areas, it is between 0.06 and 0.27 cm^3/cm^3, and the northern area is arid. This can provide valuable reference information for irrigation management. Thus, it can be concluded that SSM estimated by the model was highly consistent with in situ measured SSM. The model developed in our research is applicable for SSM estimation of farmland.

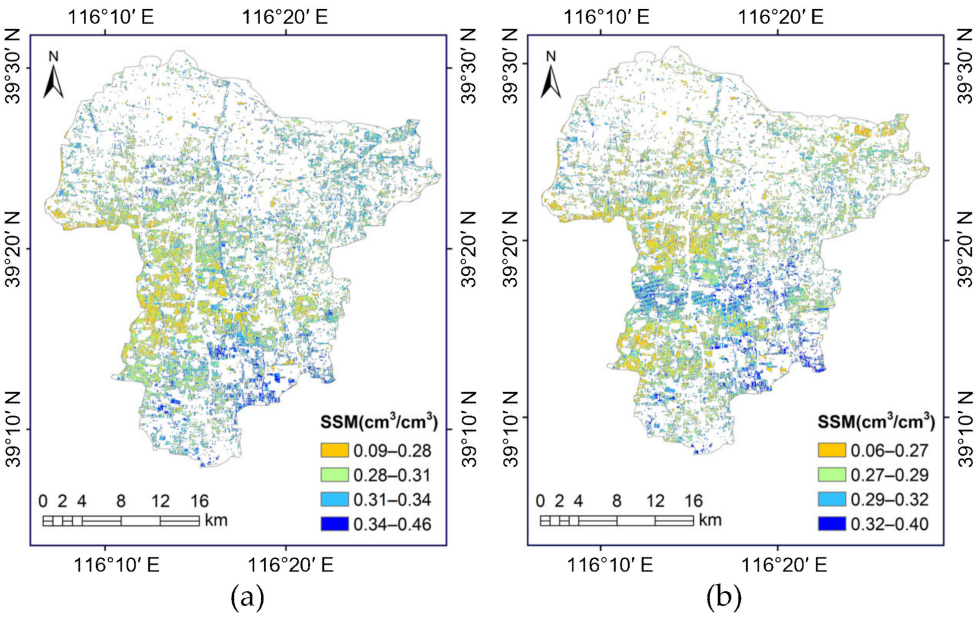

Figure 8. SSM mapping on two different dates: 28 April 2019 (**a**), and 29 April 2021 (**b**), in Gu'an, Hebei, China.

4. Discussion

4.1. SSM Estimation in Vegetated Areas

Many RS-based models are available for SSM retrieval [43–48]. However, these models have limited potential to estimate SSM directly over vegetation-covered areas due to the distributed scattering of vegetation. Microwave RS can be widely used in SSM estimation

because it is not affected by weather or light and has strong penetration, which can improve reliability and effectiveness. However, in vegetation-covered areas, the attenuation and scattering of microwave radiation signals from soil by the vegetation layer and radiation from the vegetation itself will influence the accuracy of SSM estimation. In the research of SSM retrieval, removing the effect of the vegetation layer has always been the focus, and some progress has been made.

In this paper, the WCM was used to estimate SSM in vegetation-covered areas, and satisfactory results were obtained, with an R^2 of 0.867, MAE of 0.023 cm^3/cm^3, and RMSE of 0.028 cm^3/cm^3. The results were close to those obtained in other studies. Bao et al. [40] used an improved water cloud model to estimate SSM in partial vegetation-covered areas in UK and Spain and found that the modeled value had a high consistency with the in situ measured value (R^2 = 0.829); this value was slightly lower than the validation obtained in the present study (R^2 = 0.867). This difference is mainly due to differences in the used optical RS data and the number of verification points. Bousbih et al. [14] used the WCM to estimate SSM in the Kairouan plain, and the validation results were relatively poor (R^2 = 0.4, RMSE = 0.064 cm^3/cm^3). However, it has been well applied in irrigation mapping. Gao et al. [49] obtained regional SSM with a spatial resolution of 100 m in Urgell (Catalunya, Spain) using S1 SAR and S2 optical data based on change detection and found that the modeled value had a high consistency with the in situ measured value (RMSE = 0.087 cm^3/cm^3); this value was slightly higher than the validation obtained in the present study. This difference is mainly due to differences in the spatial resolution and methods used. Santamaría-Artigas et al. [50] developed the evaluation of an optical–passive microwave method for SSM estimation at the regional scale using RS and reanalysis data. The results contribute to the use of single linear and semi-empirical regressions to calculate SSM at the regional scale based on SMOS L-band bipolarized brightness temperature. Meng et al. [51] developed an SSM retrieval algorithm from multisource fusion data through the sowing, jointing, heading, and flowering stages of maize. The results showed that the improved Dubois (IDubois) model was better than the Dubois model, based on the RMSE ($RMSE_{IDubois}$ = 0.0371 cm^3/cm^3, $RMSE_{Dubois}$ = 0.0654 cm^3/cm^3); these values were slightly higher than the validation obtained in the present study (RMSE = 0.028 cm^3/cm^3). This difference may be caused by the different models used.

Based on the above studies, it can be found that the improved WCM based on the vegetation red-edge band proposed in this research has improved accuracy with a high spatial resolution (20 m × 20 m), which has a wide application prospect.

4.2. Some Errors and Research Expectations

Section 4.1 compared relevant studies on SSM estimation in vegetated areas, and the accuracy obtained by different studies is inconsistent. Part of the bias is caused by objective factors such as the inaccuracy of the input data and the limitations of the validation methods. Meanwhile, additional bias is contributed by the subjective factor of the innate defects of the algorithms. There are also errors in this study.

On the one hand, S1 SAR and S2 MSI images have their own registration errors and correction errors, as well as spatial resolution matching errors of S1 and S2, which will affect the inversion accuracy of SSM. On the other hand, the spatial distribution of SSM has strong spatial heterogeneity, and the in situ measured sample value cannot completely objectively and truly reflect the actual situation of the 20 m spatial scale (spatial resolution of remote sensing image data resampling–sampling).

In this research, the vegetation red-edge band with a central wavelength of 0.705 μm was used to calculate the MCARI, which was used to estimate the VWC. The SSM estimation model was established, and high accuracy was obtained. However, there are four vegetation red-edge bands of the S2 satellite, and their central wavelengths are 0.705, 0.740, 0.783, and 0.865 μm, respectively, corresponding to Band 5, Band 6, Band 7, and Band 8A. The indices calculated from each vegetation red-edge band are called MCARI1, MCARI2, MCARI3, and MCARI4, respectively. That is, our research used MCARI1 without a comparative

analysis of MCARI2, MCARI3, and MCARI4. We still do not know the effects of the other three indexes on SSM estimation. In the future, the above four indices can be compared to further clarify the MCARI and which vegetation red-edge band calculated has the best performance in SSM estimation.

The SSM estimation model developed in our research is simple and easy to implement, and the estimated SSM has very satisfactory robustness at a high spatial resolution. There is no denying that the developed model also has some disadvantages that need to be addressed in the future. First, there is still some error introduced due to ignoring the surface roughness and crop type. Secondly, the transit date of the S2 satellite is not completely synchronized with the transit date of the S1 satellite. In addition, although clouds, rain, and other extreme weather conditions have little to no impact on S1 images, they have a great impact on optical remote sensing images, and the data obtained by the cloud processing algorithm is not the best choice, which may be a challenge. At present, soil moisture data sets with a high spatiotemporal resolution are still scarce. In the future, to produce a high spatiotemporal resolution products (e.g., 20 m $\times$ 20 m, daily), it is needed to make full use of MODIS and Landsat images and introduce spatiotemporal fusion methods, e.g., the Enhanced Spatial and Temporal Adaptive Reflectance Fusion Model (ESTARFM) [52], the Flexible Spatiotemporal Data Fusion (FSDAF) [53], and the Cubesat Enabled Spatio-Temporal Enhancement Method (CESTEM) [54].

5. Conclusions

The timely and accurate acquisition of SSM information is very important for agricultural water resource management and drought monitoring. Many scholars have carried out a series of studies on bare soil or sparse vegetation areas and made positive contributions to this field. However, there are relatively few studies on SSM in vegetation-covered areas such as farmland. At present, the potential of the MCARI for SSM estimation has not been exploited, and it is an important part of our research. In this paper, backscattering coefficients and spectral indices were obtained from S1 and S2 images, respectively. Then, the effectiveness of the MCARI in SSM estimation was evaluated with the WCM and compared with the other two vegetation indices (NDVI and NDWI). Finally, the model was validated with in situ measured SSM values, and the SSM of the vegetated areas in Daxing, Beijing, and Gu'an, Hebei, in two periods was plotted. The detailed conclusions of this study can be summarized as follows:

1. Compared to VH polarization, VV polarization was more suitable for SSM estimation and achieved higher accuracy.
2. The MCARI performed well in estimating the VWC, which made it show excellent potential in estimating SSM in vegetation-covered areas.
3. Based on the MCARI, the SSM estimation model was developed. The R^2, RMSE, and MAE between the estimated and in situ measured SSM values were 0.867, 0.028 cm^3/cm^3, and 0.023 cm^3/cm^3, respectively.
4. This method can obtain SSM information with a high spatial resolution, which can be used to guide agricultural irrigation and make positive contributions to agricultural water resource management and drought monitoring.

Author Contributions: Methodology, R.L.; Formal analysis, R.L., H.C. and Z.W.; Data curation, R.L., H.S. and M.C.; Funding acquisition, Z.W.; Project administration, Y.L. and B.Z. All authors have read and agreed to the published version of the manuscript.

Funding: This research was funded by the National Key Research and Development Program of China (No. 2021YFB3900602), the Chinese National Science Fund (No. 52130906), the Independent Research Project of State Key Laboratory of Simulation and Regulation of Water Cycle in River Basin (No. SKL2022TS13), and the Fund of China Institute of Water Resources and Hydropower Research (No. ID0145B022021, ID0145B052021).

Institutional Review Board Statement: Not applicable.

Informed Consent Statement: Not applicable.

Data Availability Statement: Not applicable.

Acknowledgments: We would like to thank the anonymous reviewers for their long-term guidance and constructive comments. Moreover, we are grateful to the European Space Agency (ESA) and the United States Geological Survey (USGS) for providing remote sensing (RS) images for free.

Conflicts of Interest: The authors declare no conflict of interest.

References

1. Petropoulos, G.; Srivastava, P.; Piles, M.; Pearson, S. Earth Observation-Based Operational Estimation of Soil Moisture and Evapotranspiration for Agricultural Crops in Support of Sustainable Water Management. *Sustainability* **2018**, *10*, 181. [CrossRef]
2. Dorigo, W.; Wagner, W.; Albergel, C.; Albrecht, F.; Balsamo, G.; Brocca, L.; Chung, D.; Ertl, M.; Forkel, M.; Gruber, A.; et al. ESA CCI Soil Moisture for improved Earth system understanding: State-of-the art and future directions. *Remote Sens. Environ.* **2017**, *203*, 185–215. [CrossRef]
3. Abowarda, A.S.; Bai, L.; Zhang, C.; Long, D.; Li, X.; Huang, Q.; Sun, Z. Generating surface soil moisture at 30 m spatial resolution using both data fusion and machine learning toward better water resources management at the field scale. *Remote Sens. Environ.* **2021**, *255*, 112301. [CrossRef]
4. Long, D.; Bai, L.; Yan, L.; Zhang, C.; Yang, W.; Lei, H.; Quan, J.; Meng, X.; Shi, C. Generation of spatially complete and daily continuous surface soil moisture of high spatial resolution. *Remote Sens. Environ.* **2019**, *233*, 111364. [CrossRef]
5. Whyte, A.; Ferentinos, K.P.; Petropoulos, G.P. A new synergistic approach for monitoring wetlands using Sentinels -1 and 2 data with object-based machine learning algorithms. *Environ. Modell. Softw.* **2018**, *104*, 40–54. [CrossRef]
6. Liu, Z.; Todini, E. Towards a comprehensive physically-based rainfall-runoff model. *Hydrol. Earth Syst. Sci.* **2002**, *6*, 859–881. [CrossRef]
7. Anagnostopoulos, V.; Petropoulos, G.P.; Ireland, G.; Carlson, T.N. A modernized version of a 1D soil vegetation atmosphere transfer model for improving its future use in land surface interactions studies. *Environ. Modell. Softw.* **2017**, *90*, 147–156. [CrossRef]
8. Ozdogan, M.; Gutman, G. A new methodology to map irrigated areas using multi-temporal MODIS and ancillary data: An application example in the continental US. *Remote Sens. Environ.* **2008**, *112*, 3520–3537. [CrossRef]
9. Ambika, A.K.; Wardlow, B.; Mishra, V. Remotely sensed high resolution irrigated area mapping in India for 2000 to 2015. *Sci. Data* **2016**, *3*, 160118. [CrossRef]
10. Schmugge, T.J.; Jackson, T.J.; McKim, H.L. Survey of methods for soil moisture determination. *Water Resour. Res.* **1980**, *16*, 961–979. [CrossRef]
11. Majcher, J.; Kafarski, M.; Wilczek, A.; Woszczyk, A.; Szyplowska, A.; Lewandowski, A.; Szerement, J.; Skierucha, W. Application of a Monopole Antenna Probe with an Optimized Flange Diameter for Tdr Soil Moisture Measurement. *Sensors* **2020**, *20*, 2374. [CrossRef]
12. Peng, J.; Loew, A.; Merlin, O.; Verhoest, N.E.C. A review of spatial downscaling of satellite remotely sensed soil moisture. *Rev. Geophys.* **2017**, *55*, 341–366. [CrossRef]
13. Amazirh, A.; Merlin, O.; Er-Raki, S.; Gao, Q.; Rivalland, V.; Malbeteau, Y.; Khabba, S.; Escorihuela, M.J. Retrieving surface soil moisture at high spatio-temporal resolution from a synergy between Sentinel-1 radar and Landsat thermal data: A study case over bare soil. *Remote Sens. Environ.* **2018**, *211*, 321–337. [CrossRef]
14. Bousbih, S.; Zribi, M.; El Hajj, M.; Baghdadi, N.; Lili-Chabaane, Z.; Gao, Q.; Fanise, P. Soil Moisture and Irrigation Mapping in A Semi-Arid Region, Based on the Synergetic Use of Sentinel-1 and Sentinel-2 Data. *Remote Sens.* **2018**, *10*, 1953. [CrossRef]
15. Moran, M.S.; Peters-Lidard, C.D.; Watts, J.M.; McElroy, S. Estimating soil moisture at the watershed scale with satellite-based radar and land surface models. *Remote Sens.* **2004**, *30*, 805–826. [CrossRef]
16. Wang, L.; Qu, J.J. Satellite remote sensing applications for surface soil moisture monitoring: A review. *Front. Earth Sci. China* **2009**, *3*, 237–247. [CrossRef]
17. Kumar, K.; Suryanarayana Rao, H.P.; Arora, M.K. Study of water cloud model vegetation descriptors in estimating soil moisture in Solani catchment. *Hydrol. Process.* **2015**, *29*, 2137–2148. [CrossRef]
18. Petropoulos, G.P.; Ireland, G.; Srivastava, P.K.; Ioannou-Katidis, P. An appraisal of the accuracy of operational soil moisture estimates from SMOS MIRAS using validated in situ observations acquired in a Mediterranean environment. *Int. J. Remote Sens.* **2014**, *35*, 5239–5250. [CrossRef]
19. Adams, J.R.; Berg, A.A.; McNairn, H.; Merzouki, A. Sensitivity of C-band SAR polarimetric variables to unvegetated agricultural fields. *Can. J. Remote Sens.* **2014**, *39*, 1–16. [CrossRef]
20. Paloscia, S.; Pettinato, S.; Santi, E.; Notarnicola, C.; Pasolli, L.; Reppucci, A. Soil moisture mapping using Sentinel-1 images: Algorithm and preliminary validation. *Remote Sens. Environ.* **2013**, *134*, 234–248. [CrossRef]
21. Kui, L.; Rui, Z.; Jinliang, D.; Jichao, L. Wide-area soil moisture retrieval using SAR images and multispectral data. *Trans. Chin. Soc. Agric. Eng.* **2020**, *36*, 134–140. [CrossRef]
22. Attema, E.P.W.; Ulaby, F.T. Vegetation modeled as a water cloud. *Radio Sci.* **1978**, *13*, 357–364. [CrossRef]

23. Baghdadi, N.; Hajj, M.E.; Zribi, M. Coupling SAR C-Band and Optical Data for Soil Moisture and Leaf Area Index Retrieval Over Irrigated Grasslands. *IEEE J. Sel. Top. Appl. Earth Obs. Remote Sens.* **2016**, *9*, 1229–1243. [CrossRef]
24. Gherboudj, I.; Magagi, R.; Berg, A.A.; Toth, B. Soil moisture retrieval over agricultural fields from multi-polarized and multi-angular RADARSAT-2 SAR data. *Remote Sens. Environ.* **2011**, *115*, 33–43. [CrossRef]
25. Singh Rawat, K.; Kumar Singh, S.; Kumar Pal, R. Synergetic methodology for estimation of soil moisture over agricultural area using Landsat-8 and Sentinel-1 satellite data. *Remote Sens. Appl. Soc. Environ.* **2019**, *15*, 100250. [CrossRef]
26. Baghdadi, N.; El Hajj, M.; Zribi, M.; Bousbih, S. Calibration of the Water Cloud Model at C-Band for Winter Crop Fields and Grasslands. *Remote Sens.* **2017**, *9*, 969. [CrossRef]
27. El Hajj, M.; Baghdadi, N.; Zribi, M.; Belaud, G.; Cheviron, B.; Courault, D.; Charron, F. Soil moisture retrieval over irrigated grassland using X-band SAR data. *Remote Sens. Environ.* **2016**, *176*, 202–218. [CrossRef]
28. He, B.; Xing, M.; Bai, X. A Synergistic Methodology for Soil Moisture Estimation in an Alpine Prairie Using Radar and Optical Satellite Data. *Remote Sens.* **2014**, *6*, 10966–10985. [CrossRef]
29. Bai, X.; He, B.; Li, X. Optimum Surface Roughness to Parameterize Advanced Integral Equation Model for Soil Moisture Retrieval in Prairie Area Using Radarsat-2 Data. *IEEE Trans. Geosci. Remote Sens.* **2016**, *54*, 2437–2449. [CrossRef]
30. Huang, Y.; Walker, J.P.; Gao, Y.; Wu, X.; Monerris, A. Estimation of Vegetation Water Content From the Radar Vegetation Index at L-Band. *IEEE Trans. Geosci. Remote Sens.* **2016**, *54*, 981–989. [CrossRef]
31. Chen, D.; Huang, J.; Jackson, T.J. Vegetation water content estimation for corn and soybeans using spectral indices derived from MODIS near- and short-wave infrared bands. *Remote Sens. Environ.* **2005**, *98*, 225–236. [CrossRef]
32. Daughtry, C.; Walthall, C.L.; Kim, M.S.; Colstoun, E.; Iii, M.M. Estimating Corn Leaf Chlorophyll Concentration from Leaf and Canopy Reflectance. *Remote Sens. Environ.* **2000**, *74*, 229–239. [CrossRef]
33. Han, X.; Xiuwan, C.; Zhenyu, Y.; Huaiyu, L.; Han, Z. Vegetation Index Estimation by Chlorophyll Content of Grassland Based on Spectral Analysis. *Spectrosc. Spect. Anal.* **2014**, *34*, 3075–3078. [CrossRef]
34. Zhao, Y.; Zhang, X.; Bai, Y.; Mi, F. Does Land Use Change Affect Green Space Water Use? An Analysis of the Haihe River Basin. *Forests* **2019**, *10*, 545. [CrossRef]
35. Han, Y.; Jia, D.; Zhuo, L.; Sauvage, S.; Sánchez-Pérez, J.-M.; Huang, H.; Wang, C. Assessing the Water Footprint of Wheat and Maize in Haihe River Basin, Northern China (1956–2015). *Water* **2018**, *10*, 867. [CrossRef]
36. El Hajj, M.; Baghdadi, N.; Zribi, M.; Bazzi, H. Synergic Use of Sentinel-1 and Sentinel-2 Images for Operational Soil Moisture Mapping at High Spatial Resolution over Agricultural Areas. *Remote Sens.* **2017**, *9*, 1292. [CrossRef]
37. Prakash, R.; Singh, D.; Pathak, N.P. A Fusion Approach to Retrieve Soil Moisture With SAR and Optical Data. *IEEE J. Sel. Top. Appl. Earth Obs. Remote Sens.* **2012**, *5*, 196–206. [CrossRef]
38. Huang, J.; Chen, D.; Cosh, M.H. Sub-pixel reflectance unmixing in estimating vegetation water content and dry biomass of corn and soybeans cropland using normalized difference water index (NDWI) from satellites. *Int. J. Remote Sens.* **2009**, *30*, 2075–2104. [CrossRef]
39. Jackson, T. Vegetation water content mapping using Landsat data derived normalized difference water index for corn and soybeans. *Remote Sens. Environ.* **2004**, *92*, 475–482. [CrossRef]
40. Bao, Y.; Lin, L.; Wu, S.; Kwal Deng, K.A.; Petropoulos, G.P. Surface soil moisture retrievals over partially vegetated areas from the synergy of Sentinel-1 and Landsat 8 data using a modified water-cloud model. *Int. J. Appl. Earth Obs. Geoinf.* **2018**, *72*, 76–85. [CrossRef]
41. Mattia, F.; Satalino, G.; Dente, L.; Pasquariello, G. Using a priori information to improve soil moisture retrieval from ENVISAT ASAR AP data in semiarid regions. *IEEE Trans. Geosci. Remote Sens.* **2006**, *44*, 900–912. [CrossRef]
42. Van der Schalie, R.; de Jeu, R.A.M.; Kerr, Y.H.; Wigneron, J.P.; Rodríguez-Fernández, N.J.; Al-Yaari, A.; Parinussa, R.M.; Mecklenburg, S.; Drusch, M. The merging of radiative transfer based surface soil moisture data from SMOS and AMSR-E. *Remote Sens. Environ.* **2017**, *189*, 180–193. [CrossRef]
43. Rawat, K.S.; Singh, S.K. Estimation of Surface Runoff from Semi-arid Ungauged Agricultural Watershed Using SCS-CN Method and Earth Observation Data Sets. *Water Conserv. Sci. Eng.* **2017**, *1*, 233–247. [CrossRef]
44. Zribi, M.; Dechambre, M. A new empirical model to retrieve soil moisture and roughness from C-band radar data. *Remote Sens. Environ.* **2003**, *84*, 42–52. [CrossRef]
45. Bala, A.; Rawat, K.S.; Misra, A.K.; Srivastava, A. Assessment and validation of evapotranspiration using SEBAL algorithm and Lysimeter data of IARI agricultural farm, India. *Geocarto Int.* **2015**, *31*, 739–764. [CrossRef]
46. Chen, K.S.; Tzong-Dar, W.; Leung, T.; Qin, L.; Jiancheng, S.; Fung, A.K. Emission of rough surfaces calculated by the integral equation method with comparison to three-dimensional moment method simulations. *IEEE Trans. Geosci. Remote Sens.* **2003**, *41*, 90–101. [CrossRef]
47. Oh, Y.; Sarabandi, K.; Ulaby, F.T. An Empirical Model and an Inversion Technique for Radar Scattering from Bare Soil Surfaces. *IEEE Trans. Geosci. Remote Sens.* **1992**, *30*, 370–381. [CrossRef]
48. Fung, A.K.; Chen, K.S. An Update on the IEM Surface Backscattering Model. *IEEE Geosci. Remote Sens. Lett.* **2004**, *1*, 75–77. [CrossRef]
49. Gao, Q.; Zribi, M.; Escorihuela, M.J.; Baghdadi, N. Synergetic Use of Sentinel-1 and Sentinel-2 Data for Soil Moisture Mapping at 100 m Resolution. *Sensors* **2017**, *17*, 1966. [CrossRef] [PubMed]

50. Santamaria-Artigas, A.; Mattar, C.; Wigneron, J.-P. Application of a Combined Optical–Passive Microwave Method to Retrieve Soil Moisture at Regional Scale Over Chile. *IEEE J. Sel. Top. Appl. Earth Obs. Remote Sens.* **2016**, *9*, 1493–1504. [CrossRef]
51. Meng, Q.; Xie, Q.; Wang, C.; Ma, J.; Sun, Y.; Zhang, L. A fusion approach of the improved Dubois model and best canopy water retrieval models to retrieve soil moisture through all maize growth stages from Radarsat-2 and Landsat-8 data. *Environ. Earth Sci.* **2016**, *75*, 1377. [CrossRef]
52. Kong, J.; Ryu, Y.; Huang, Y.; Dechant, B.; Houborg, R.; Guan, K.; Zhu, X. Evaluation of four image fusion NDVI products against in-situ spectral-measurements over a heterogeneous rice paddy landscape. *Agric. For. Meteorol.* **2021**, *297*, 108255. [CrossRef]
53. Zhu, X.; Helmer, E.H.; Gao, F.; Liu, D.; Chen, J.; Lefsky, M.A. A flexible spatiotemporal method for fusing satellite images with different resolutions. *Remote Sens. Environ.* **2016**, *172*, 165–177. [CrossRef]
54. Houborg, R.; McCabe, M.F. A Cubesat enabled Spatio-Temporal Enhancement Method (CESTEM) utilizing Planet, Landsat and MODIS data. *Remote Sens. Environ.* **2018**, *209*, 211–226. [CrossRef]